

Ultrahigh Energy Nuclei in the Turbulent Galactic Magnetic Field

G. Giacinti^{a,b}, M. Kachelrieß^c, D. V. Semikoz^{a,d}, G. Sigl^b

^a*AstroParticle and Cosmology (APC), Paris, France*

^b*II. Institut für Theoretische Physik, Universität Hamburg, Germany*

^c*Institutt for fysikk, NTNU, Trondheim, Norway*

^d*Institute for Nuclear Research of the Russian Academy of Sciences, Moscow, Russia*

Abstract

In this work we study how the turbulent component of the Galactic magnetic field (GMF) affects the propagation of ultrahigh energy heavy nuclei. We investigate first how the images of individual sources and of the supergalactic plane depend on the properties of the turbulent GMF. Then we present a quantitative study of the impact of the turbulent field on (de-) magnification of source fluxes, due to magnetic lensing effects. We also show that it is impossible to explain the Pierre Auger data assuming that all ultrahigh energy nuclei are coming from Cen A, even in the most favorable case of a strong, extended turbulent field in the Galactic halo.

Keywords: Ultrahigh energy cosmic rays, Galactic magnetic fields.

1. Introduction

The composition of the cosmic ray (CR) flux above energies $E \gtrsim 10^{17}$ eV is a topic of current debate. The shape of the CR spectrum [1, 2, 3] at the highest energies is compatible with either a proton or a heavy nuclei composition. On the one hand, the correlation of ultrahigh energy cosmic rays (UHECRs) arrival directions with the large scale distribution of active galactic nuclei reported by the Pierre Auger collaboration [4, 5] could be consistent with a composition dominated by protons. On the other hand, the possibility to accelerate nuclei to higher energies as protons may favour a transition to heavier nuclei at the end of the UHECR spectrum. Meanwhile, various results of measurements of the UHECR composition have been presented: The Pierre Auger Observatory air shower measurements suggest a gradual shift towards a heavier composition starting at a few times 10^{18} eV up to $\approx 4 \times 10^{19}$ eV above which the statistics is currently still insufficient for composition studies [6]. The Yakutsk EAS Array muon data are compatible with this result [7]. However, both HiRes measurements [8] and preliminary studies of the Telescope Array [9] do not agree with this shift. The results of their composition studies favour proton primaries.

In this work, we extend our previous analysis of the implications of a possible heavy primary composition on the UHECRs propagation in the Galactic magnetic field (GMF) [10]: We add a *turbulent* component to the regular GMF and investigate in details its influence. We present in this paper simulations for iron nuclei with the energy $E = 60$ EeV, since this is the highest energy where present experiments collect still a reasonable number of events.

T. Stanev suggested one of the first models of the regular GMF including a spiral arm-like structure of the field in

the Galactic disk [11]. Other models were later proposed in Refs. [12, 13]. The authors of Refs. [14] and [15] presented a toroidal field consisting of concentric rings and another axisymmetric field, respectively. Spiral patterns based either on the structure of the NE2001 thermal electron density model [16] or on the spiral structure of the Milky Way [17] deduced from HII regions and giant molecular clouds [18] have also been proposed to describe this field. The implications on the GMF modelling of recent rotation measure maps were reported in [19, 20, 21]. Some of the most recent constraints on the regular disk field have been presented in [22, 23, 24].

The authors of Ref. [25] presented first a GMF model adding a halo contribution made of toroidal and poloidal fields to the disk field [25, 26]. In the present paper, we refer to this model as the “PS model”. Several new GMF models were proposed and confronted with the data in Refs. [27, 28, 29]. At present, no theoretical GMF model can fit all experimental data [30, 31].

Earlier works discussing the propagation of UHECRs in turbulent fields include Refs. [32, 33]. The first studied the generic theoretical properties of multiple image formation and amplification in a turbulent magnetic field for point-like UHECR sources [32]. Ref. [33] discussed the range of values one could expect for the relative ratios of UHECR deflections in the regular and turbulent GMF. In our present work, we deal with the case of iron nuclei at the highest energies emitted by extended extragalactic sources considering both the regular and the turbulent components of the GMF.

Our paper is structured as follows: Section 2 presents and discusses the two numerical methods that we use to generate the turbulent GMF. In Section 3, we investigate qualitatively the consequences induced by the turbulent GMF on the shape of images of single sources and of the supergalactic plane. The implications of this field on the (de-) magnification of the fluxes from single sources are presented in Section 4. In Section 5,

Email address: giacinti@apc.univ-paris7.fr (G. Giacinti)

we rule out the possibility that all presently observed UHECR events could have been emitted by only one nearby source and deflected over the celestial sphere by a strong turbulent-dominated GMF.

2. Modelling of the turbulent Galactic magnetic field

In this section, we present the two methods we use to model the turbulent Galactic magnetic field and recall some of its basic properties. A turbulent magnetic field \mathbf{B} satisfies $\langle \mathbf{B}(\mathbf{r}) \rangle = \mathbf{0}$ and $\langle \mathbf{B}^2(\mathbf{r}) \rangle \equiv B_{\text{rms}}^2 > 0$. At the energy we consider throughout this work, $E = 60$ EeV, the Larmor radius of iron primaries is typically much larger than the coherence length L_c of the turbulent field. As a result, the effect of a uniform turbulent field can be parametrised in this regime by L_c and B_{rms} . Therefore, our results for the deflections are largely independent of the exact shape of the fluctuation spectrum which is poorly constrained. In the following we will consider for definiteness a Kolmogorov spectrum. If k denotes the modulus of wave vectors, the power spectrum of such a field is $\mathcal{P}(k) \propto k^{-5/3}$ and the amplitudes $\mathbf{B}(\mathbf{k})$ of its Fourier modes follow $|\mathbf{B}(\mathbf{k})|^2 \propto k^{-11/3}$.

The modulus of wave vectors \mathbf{k} in Fourier space satisfy $2\pi/L_{\text{max}} \leq k = |\mathbf{k}| \leq 2\pi/L_{\text{min}}$, where L_{min} and L_{max} denote the minimal and the maximal scales of variation present in the field $\mathbf{B}(\mathbf{r})$, respectively. The correlation length L_c of the field is equal to

$$L_c = \frac{1}{5} L_{\text{max}} \frac{1 - (L_{\text{min}}/L_{\text{max}})^{5/3}}{1 - (L_{\text{min}}/L_{\text{max}})^{2/3}}. \quad (1)$$

Turbulent magnetic fields can be generated either directly in coordinate space as a superposition of a finite number of plane waves, or by computing the field on a three-dimensional grid using the Fast Fourier Transform (FFT). In the present paper we use the first method in Sections 3 and 4 following Ref. [34]. The field $\mathbf{B}(\mathbf{r})$ is written as the sum of N_m modes,

$$\mathbf{B}(\mathbf{r}) = \sum_{n=1}^{N_m} A_n \varepsilon_n \exp(i\mathbf{k}_n \cdot \mathbf{r} + i\beta_n), \quad (2)$$

where $\varepsilon_n = \cos(\alpha_n)\widehat{\mathbf{x}}_n + i\sin(\alpha_n)\widehat{\mathbf{y}}_n$, α_n and β_n represent random phases and the unit vectors $\widehat{\mathbf{x}}_n$ and $\widehat{\mathbf{y}}_n$ form an orthogonal basis together with the randomly chosen direction of the n -th wave vector \mathbf{k}_n . The amplitude A_n of the n -th plane wave is given by

$$A_n^2 = \frac{B_{\text{rms}}^2 G(\mathbf{k})}{\sum_{n=1}^{N_m} G(\mathbf{k}_n)}, \quad (3)$$

with

$$G(\mathbf{k}) = \frac{4\pi k^2 \Delta k}{1 + (kL_c)^{11/3}}. \quad (4)$$

We choose k_n between $k_{\text{min}} = 2\pi/L_{\text{max}}$ and $k_{\text{max}} = 2\pi/L_{\text{min}}$ with equal spacings in logarithmic scale: $\Delta \log k = \Delta k/k = \text{const}$. The number of modes is set to $N_m = 1000$. We verified that with this we obtain the theoretically expected deflections in the small-angle scattering regime with an error smaller than $\simeq 2\%$. Once the modes are dialed, the turbulent field can be

computed with Eq. (2) at any point in space with arbitrary precision for the given realization. Its drawback is that computations are much slower than with the second method described below, because the method requires to compute many trigonometric functions at each step of the particle trajectory.

The second method consists in precomputing the field on a three dimensional grid in real space. The coordinates of its wave vectors correspond to positions of vertices on the reciprocal grid in the Fourier space. The resulting field in real space is computed with the Fast Fourier Transform (FFT) [35]. The magnetic field can be quickly interpolated at any point of the space. We take an 8 point-interpolation of the field values on the eight vertices of the grid cell in which the considered point lies.

We use this method in Section 5 to derive results which require the propagation of 3.6×10^6 particles. For this work, using a three dimensional cubic grid of $N = 2^8$ vertices per side is sufficient. It contains 256^3 values for each component of the turbulent field. This grid of $\simeq 2.6$ kpc lateral size is periodically repeated in real space.

In the three following sections, we use the same type of generic profile for the rms strength of the turbulent field, $B_{\text{rms}}(r, z)$. We take the model introduced in Ref. [36],

$$B_{\text{rms}}(r, z) = B(r) \exp\left(-\frac{|z|}{z_0}\right), \quad (5)$$

where r is the galactocentric radius and z the distance to the Galactic plane. The parameter z_0 characterizes the extension of the random field in the halo. In the next sections, we will vary z_0 in the range 0.75 kpc to 10 kpc. The radial profile $B(r)$ is defined as

$$B(r) = \begin{cases} B_0 \exp\left(\frac{5.5}{8.5}\right) & , \text{ if } r \leq 3 \text{ kpc (bulge)} \\ B_0 \exp\left(\frac{-(r-8.5 \text{ kpc})}{8.5 \text{ kpc}}\right) & , \text{ if } r > 3 \text{ kpc} \end{cases} \quad (6)$$

where B_0 denotes the value of B_{rms} close to the Sun. For the regular field, we use the PS model choosing the parameters as described in Ref. [10].

3. Qualitative consequences of deflections in the turbulent GMF for source searches

We investigate here qualitatively the influence of the turbulent GMF on the images of single sources and the supergalactic plane emitting 60 EeV iron nuclei. Since the characteristic properties of the turbulent GMF are still poorly known, we test the dependence of the results on its main parameters.

The shape of proton and light nuclei source images has been discussed in Refs. [37, 36]. We have shown in Ref. [10] how images of extragalactic UHECR sources would look like at Earth for different models of the regular GMF for a heavy primary composition. Contrary to proton sources, one expects that some iron sources have several images even at the highest energies. Moreover, some of them may be strongly magnified or demagnified [12, 38, 39, 10]. We investigate below the impact of a non-zero turbulent GMF contribution on such results.

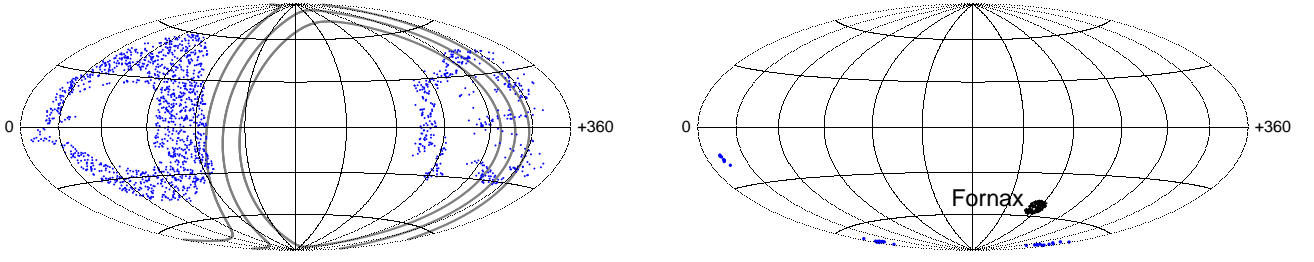


Figure 1: Images of the supergalactic plane (**left panel**) and of the Fornax galaxy cluster (**right panel**), respectively considered as a $\pm 10^\circ$ band in supergalactic latitude and a 5° radius disk, emitting 60 EeV iron nuclei deflected in the PS regular GMF model. No turbulent magnetic field was added. Dark blue points represent arrival directions of cosmic rays. The grey lines stand for the supergalactic plane and the $\pm 10^\circ$ circles in supergalactic latitude. The black disk represents Fornax. The maps are in Galactic coordinates with the anti-Galactic center in the center. Increasing l from the left to the right.

We use the model discussed in Section 2 for the profile of the rms strength of the turbulent field B_{rms} . For the regular GMF, we use the PS model as a generic example. Images of given UHECR sources can strongly vary from one GMF model to another. However, global properties of the whole sky such as mean deflection angles or fractions of the sky with given (de-)magnification [10] are similar in most recent regular GMF models. In this respect, the PS model is representative for a generic regular GMF model.

Large scale structure MHD simulations agree that extragalactic magnetic fields tend to be strongest in the large scale structure, around the largest matter concentrations [40, 41, 42, 43, 44]. However, they disagree on some aspects such as the filling factor distributions (*i.e.* the fraction of space filled with fields above a given strength, as a function of that strength [45]). This leads to substantial differences on the sizes of UHECR deflections predicted by different models, ranging from negligible [40, 41] to more than ten degrees for proton primaries, even at the very highest energies [42, 45]. Despite this, even in the case of strong deflections, UHECR would still preferentially arrive from directions towards the large scale structure (LSS) of the galaxy distribution. Since the fields in the voids are very small, UHECR arrival directions outside the Galaxy should point back to the supergalactic plane, even if they do not point back to their sources. Therefore, if sources are located in the LSS and if extragalactic deflections are sizable, it is sufficient in a first approximation to study the image of the supergalactic plane itself.

We show in Figs. 1–4 the 60 EeV iron nuclei images of the whole supergalactic plane (left columns) and of a specific galaxy cluster, Fornax (right columns).

For the images of the supergalactic plane, we assume that the region containing most of the local distribution of matter has supergalactic latitudes b_{SG} between ± 10 degrees. Cosmic ray arrival directions at Earth are represented in the figures by dark blue points, and the three grey lines correspond to the supergalactic plane ($b_{SG} = 0^\circ$) and the $b_{SG} = \pm 10^\circ$ circles. The 60 EeV iron image of the supergalactic plane in the PS model is split into two. The regions of the supergalactic plane near both Galactic poles cross blind regions and therefore do not contribute to the image observed at Earth, see Fig. 5 (upper left

panel). This cuts the supergalactic plane (SGP) into two parts: The part of the plane located at $l \sim 120^\circ - 150^\circ$ mostly produces the image at $l \sim 0^\circ - 130^\circ$, and the part at $l \sim 300^\circ - 330^\circ$ is responsible for the image at $l \sim 250^\circ - 350^\circ$. At energies $E \gtrsim 120$ EeV, the two images start to merge. In the recent GMF models presented in Refs. [27, 29], the 60 EeV iron nuclei images of the SGP display several common features. The largest part of the image(s) also appear in the region $l \sim 0^\circ - 180^\circ$, as for the PS model, and the largest contributor to this image is the part of the SGP which is located at $l \sim 120^\circ - 150^\circ$. In all tested models, the overall geometry of the image in the $l \sim 0^\circ - 180^\circ$ region is “circle-like” as for the PS model. The image may be enlarged and shifted on the sky by more than 30° from one model to another, and its details are model-dependent.

For the galaxy cluster images, we choose the Fornax cluster because its high Galactic latitude (in absolute values) avoids complicated images due to the magnetic field in the Galactic disk. In the PS model, 60 EeV iron images from the two nearby clusters with higher latitudes, Virgo and Coma, turn out to be invisible at Earth due to their strong demagnification [10]. Fornax is regarded here as a source extending over a 5° radius. Even in the case the cluster would contain only one source, deflections by magnetic fields inside the cluster lead to an extended source [46]. For the galaxy cluster images, we also assume that deflections of UHECR nuclei in extragalactic magnetic fields are weak enough (as in, e.g. the simulations of Refs. [40, 41]) that the UHECRs are not spread out over large regions of the LSS. In the figures, the cluster is denoted by a black disk.

To generate these figures, we backtrace 10^4 iron antinuclei emitted isotropically from the Earth to the outside of the Galactic halo. We record those which escape the Galaxy in directions in the $b_{SG} = -10^\circ$ to $+10^\circ$ band for the supergalactic plane images, and within 5 degrees from the center of Fornax for the Fornax images.

Figure 1 presents the supergalactic plane and Fornax images, deflected in the PS regular GMF only. This figure can be considered as the reference to which Figs. 2–4 should be compared.

For Figs. 2, 3 and 4, a non-zero turbulent GMF component was added to the PS regular component. They show the dependence of the deflections on the turbulent field rms amplitude B_0 ,

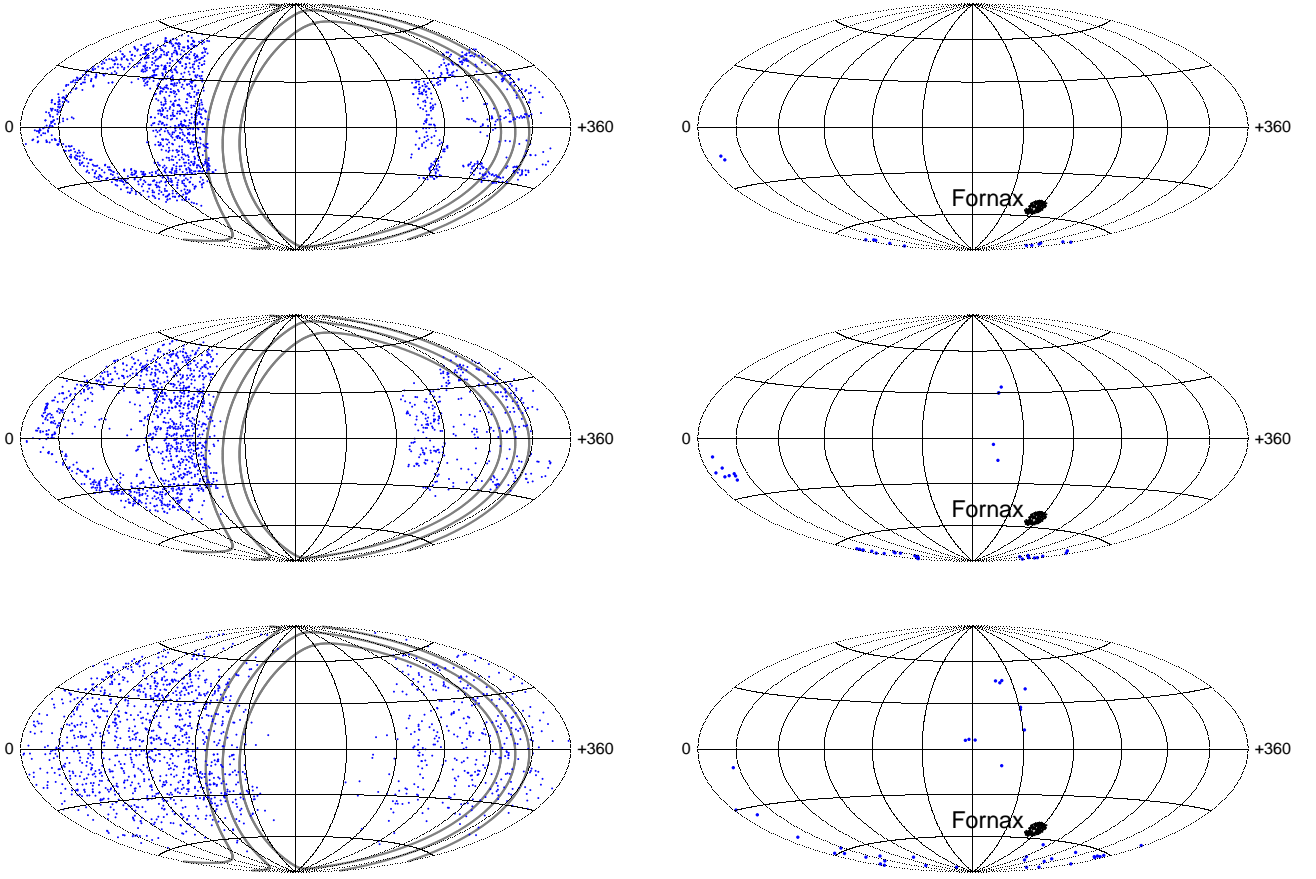


Figure 2: Impact of the turbulent field strength at Earth B_0 on the 60 EeV iron nuclei images of the supergalactic plane (**left column**), and of the Fornax galaxy cluster (**right column**). Same GMF regular component as for Fig. 1 (PS model), with in addition a non-zero turbulent Galactic magnetic field. It has a Kolmogorov spectrum of correlation length $L_c = 50$ pc. Its extension into the halo is $z_0 = 3$ kpc. See text for details on the field profile. **First row:** $B_0 = 0.25 \mu\text{G}$; **Second row:** $B_0 = 1 \mu\text{G}$; **Third row:** $B_0 = 4 \mu\text{G}$. Same key as for Fig. 1.

its correlation length L_c and its extension above the Galactic plane z_0 . For clarity, we choose a given “reference” configuration of the turbulent field parameters $\{B_0, L_c, z_0\}$, and for each figure, only one parameter varies, while the two others are fixed to the reference values for which we take $B_0 = 1 \mu\text{G}$, $z_0 = 3$ kpc and $L_c = 50$ pc. This configuration corresponds to the second row in Fig. 2. For all examples presented in this work, we adopt a Kolmogorov spectrum with $L_{\min} = 0.4 L_c$ and $L_{\max} = 4 L_c$.

Each plot shown in this section is computed for one given realisation of the turbulent field. We have checked that the results would not be qualitatively different if one takes another realisation of the turbulent GMF. The only exception to this is the lower row in Fig. 3, for the turbulent field with $L_c = 200$ pc and $z_0 = 3$ kpc. Since z_0 is not much larger than L_{\max} , cosmic rays are more sensitive to the given realisation of the field.

In Fig. 2, each row corresponds to a different strength of the turbulent GMF. From the top to the bottom, the field value at Earth B_0 is respectively set to $0.25 \mu\text{G}$, $1 \mu\text{G}$ and $4 \mu\text{G}$. The effect of this parameter is easily visible both in the Fornax and supergalactic plane images. When the turbulent field strength is increased, the images are more and more spread out, compared to those in Fig. 1. For example, the angular spread of the

Fornax image at $(l \sim 0^\circ, b \sim -70^\circ)$ increases from negligible to nearly comparable to the magnitude of the deflection in the regular field itself. At the same time, the “center” of the image stays at the same place as in the regular field. On the two last rows, a few cosmic rays are even deflected to the northern Galactic hemisphere. For the case $B_0 = 4 \mu\text{G}$, the structure of the supergalactic plane image becomes practically unrecognizable. For this regular GMF model and the parameters of the turbulent component considered here, deflections are however still not sufficiently large to spread the image over the whole celestial sphere.

Fig. 3 presents the impact of the correlation length L_c . In the first row, L_c is 4 times smaller than the reference value, $L_c = 12.5$ pc. Images are less extended and more compact than in the case $L_c = 50$ pc. They nearly resemble to the images in Fig. 1, computed without any turbulent field. On the second row, L_c is set to 200 pc. The spread of the images is larger.

In Fig. 4, we investigate the impact of the turbulent field extension into the Galactic halo. The first and second rows respectively represent the cases $z_0 = 0.75$ kpc and $z_0 = 6$ kpc. The fine structure of the images is indeed more spread for $z_0 = 6$ kpc than for $z_0 = 0.75$ kpc, but the effect is less remarkable than the

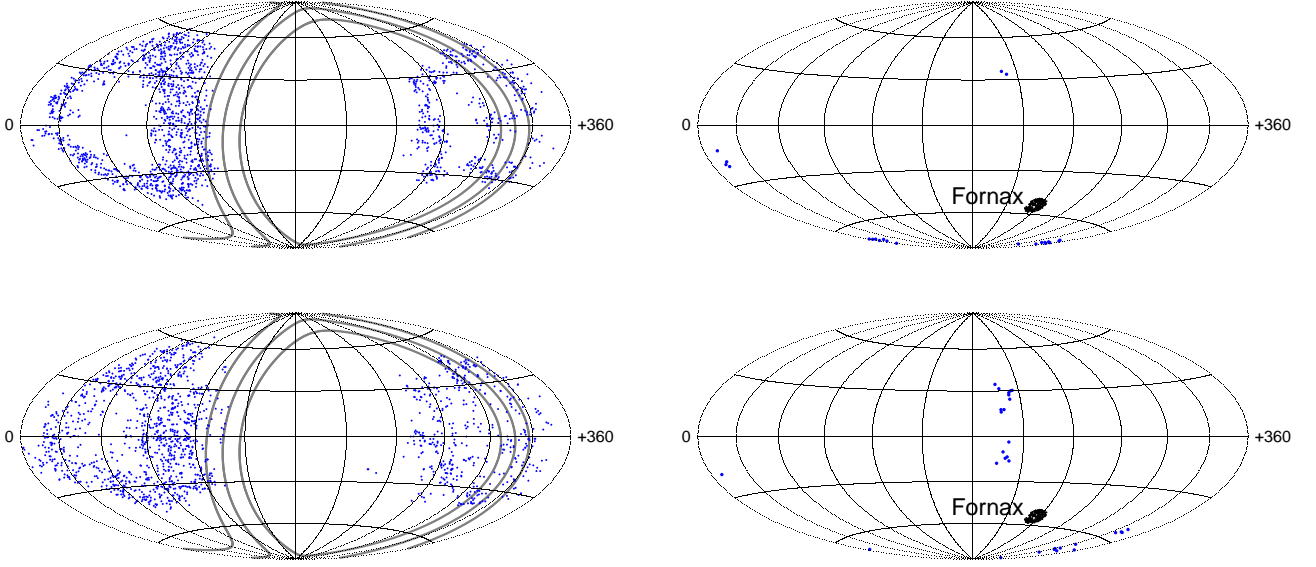


Figure 3: Columns and key as in Fig. 2. Impact of the turbulent Galactic magnetic field correlation length L_c on the supergalactic plane and Fornax 60 EeV iron images. Turbulent field with a Kolmogorov spectrum, $B_0 = 1 \mu\text{G}$ and $z_0 = 3 \text{ kpc}$. See text for details on the field profile. **First row:** $L_c = 12.5 \text{ pc}$; **Second row:** $L_c = 200 \text{ pc}$. PS model for the regular Galactic magnetic field.

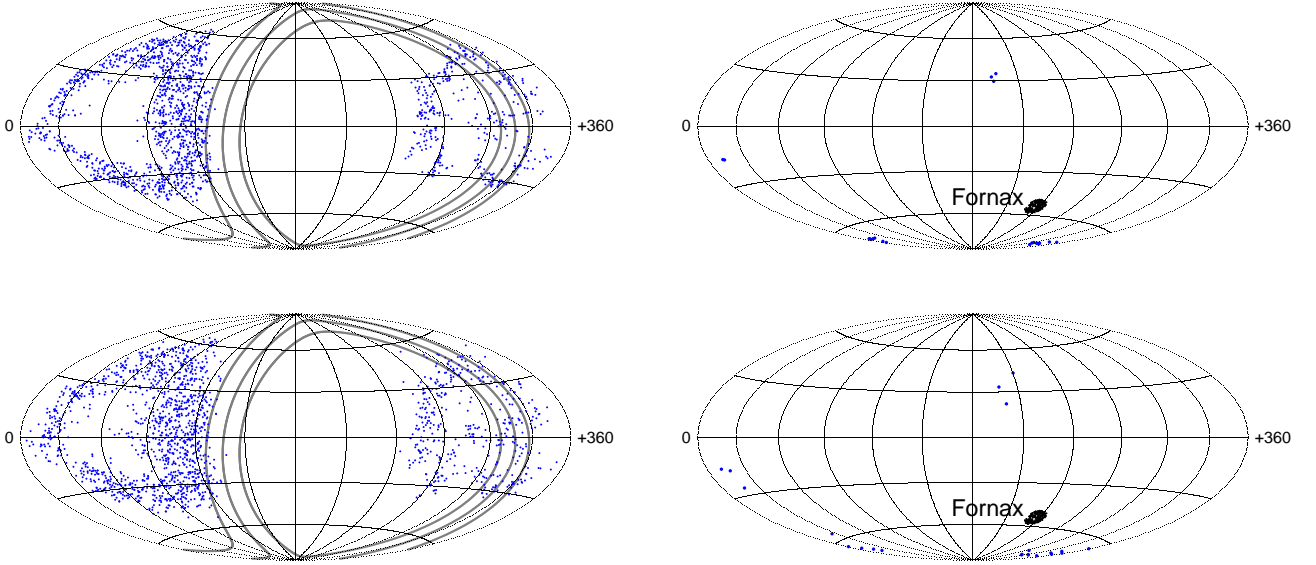


Figure 4: Columns and key as in Fig. 2. Impact of the turbulent Galactic magnetic field extension into the halo z_0 on the supergalactic plane and Fornax 60 EeV iron images. Turbulent field with a Kolmogorov spectrum of correlation length $L_c = 50 \text{ pc}$, and $B_0 = 1 \mu\text{G}$. See text for details on the field profile. **First row:** $z_0 = 0.75 \text{ kpc}$; **Second row:** $z_0 = 6 \text{ kpc}$. PS model for the regular Galactic magnetic field.

dependence on B_0 in Fig. 2.

The mean deflections in the turbulent field grow with B_0 , L_c and z_0 . In the limit case of propagation in the ballistic regime, the rms deflection δ_{rms} for particles of rigidities E/Z propagating the distance L in a turbulent field of constant rms strength B_{rms} is equal to

$$\delta_{\text{rms}} = \frac{1}{\sqrt{2}} \frac{ZeB_{\text{rms}}}{E} (LL_c)^{1/2}$$

$$\simeq 6.3^\circ \times \frac{Z}{26} \frac{60 \text{ EeV}}{E} \frac{B_{\text{rms}}}{1 \mu\text{G}} \left(\frac{L}{3 \text{ kpc}} \right)^{1/2} \left(\frac{L_c}{50 \text{ pc}} \right)^{1/2}. \quad (7)$$

If both the source and its image are located on the same side of the Galactic plane and at high enough Galactic latitudes, the distortion of the image follows the simple expectation of Eq. (7). The image of Fornax at $(l \sim 0^\circ, b \sim -70^\circ)$ is a good illustration of this dependence on the turbulent field parameters -see Figs. 1–4. In this case, iron nuclei from one given source

with $E \gtrsim 60$ EeV are more or less spread around the arrival directions that they would have had in the regular field only. Because of the linear dependence on B_{rms} , the size of the spread is more sensitive to a relative change of B_0 than to a change of L_c or z_0 .

Contrary to this simple case, if the source or its image is located at “low” Galactic latitudes ($|b| \lesssim 30 - 40^\circ$), even relatively small changes of trajectory due to the turbulent field can lead to very large distortions of the image. Some images may even appear in completely different locations. Such a behavior can be seen for the image of Fornax at ($l \sim 15^\circ, b \sim -15^\circ$), see Fig. 1. Depending on the parameters of the turbulent magnetic field, this image is partly -or completely- shifted in other parts of the sky, and new images with Galactic latitudes $|b| \lesssim 40^\circ$ appear -see Figs. 2–4. Such effects cannot be described by the simple analytical formula of Eq. (7). A full study requires the numerical computations conducted in this work.

For the ranges of turbulent GMF parameters considered here, we find no noticeable qualitative difference on source images between a field with a Kolmogorov spectrum and a field with the same modulus for all wave vectors \mathbf{k} in Fourier space, *i.e.* $L_{\text{min}} = L_{\text{max}} = 2L_c$, as long as the fields have the same correlation length.

For such parameters, iron nuclei from a source with $E \gtrsim 60$ EeV are not sufficiently spread to cover the whole sky. However, if one takes the extreme case of a very strong field, $B_0 = 10 \mu\text{G}$, extending very far into the halo, $z_0 = 10$ kpc, both the images of single sources and of the supergalactic plane are spread over the whole sky. Therefore, we investigate in Section 5 if the Pierre Auger data published recently [5] may be compatible with only one nearby UHECR source, such as Cen A, in case of a very strong and extended turbulent GMF.

4. Flux (de-) magnification of sources and extension of blind regions

In this section, we investigate the impact of the turbulent GMF on the (de-) magnification of individual source fluxes. Magnification and demagnification effects are due to magnetic lensing of UHECR in the GMF. In Ref. [10], we studied the contribution of the regular GMF component. We have shown that in the case of iron primaries, source fluxes can be strongly magnified or demagnified even for energies as high as 60 EeV. In particular, we found large regions of the sky which can be considered empty for a given number of backtraced nuclei: For instance, regions with an under-density $\rho/\langle\rho\rangle < 10^{-2.5}$ can encompass one fifth of the sky. Thus sources located in these parts of the sky would not be detectable at Earth by current and next generation UHECR experiments. We now study how these previous conclusions are affected by the turbulent component of the GMF.

The sky maps in Fig. 5 show the logarithm of the flux amplification factor \mathcal{A} of extragalactic 60 EeV iron nuclei sources, depending on their positions on the sky. We take the PS model for the regular GMF. We use the same method as in Ref. [10] to compute \mathcal{A} : We isotropically inject 10^5 iron antinuclei at Earth and backtrace them to the border of the Galaxy. Their relative

densities on the celestial sphere outside the Galaxy correspond to \mathcal{A} . These densities are computed on 3° radius circles covering the whole sky.

Let us call here “blind regions” the regions of the extragalactic sky in which $\log_{10}(\mathcal{A}) \leq -2$ for a given energy. At this energy, sources located in such regions of the sky cannot be seen at Earth by current or next generation UHECR experiments, due to the strong demagnification of their fluxes. In general, the places, extensions and shapes of blind regions do not change abruptly with energy but vary continuously with energy. For instance the blind regions in the PS model at 80 EeV are similar to those at 60 EeV, though slightly less extended. In Fig. 5, we plot blind regions in black. The amplification is below 10^{-2} in some places.

The upper left panel in Fig. 5 represents the reference plot in which the turbulent field is set to zero. In the three other panels, a turbulent component with $L_c = 50$ pc is added to the regular field. Its strength and extension in the halo are, respectively, equal to ($B_0 = 1 \mu\text{G}$, $z_0 = 3$ kpc), ($B_0 = 4 \mu\text{G}$, $z_0 = 3$ kpc) and ($B_0 = 10 \mu\text{G}$, $z_0 = 10$ kpc), for the upper right, lower left and lower right panels.

Figure 5 shows that when the amplitude and the spatial extension of the turbulent GMF halo are increased, the extension of regions of extreme magnification and demagnification tend to shrink. For example, the reduction of the size of the darkest and brightest regions from the upper left to the lower left panels is clearly visible. For the lower right panel (extremely strong and extended turbulent field), regions with $-0.5 \leq \log_{10}(\mathcal{A}) \leq 0.5$ encompass $\approx 80\%$ of the sky. This means that in $\approx 80\%$ of the sky, 60 EeV iron nuclei sources would have their fluxes neither magnified or demagnified by more than a factor ≈ 3 . In the case without any turbulent field, this fraction of the sky with moderate flux modification falls to $\approx 55\%$. Blind regions even disappear in the lower right panel.

Figure 6 (left panel) shows four histograms corresponding to the four cases shown in Fig. 5. The histograms represent the fractions of the sky with given amplifications \mathcal{A} . These histograms are computed for 10^5 backtraced antinuclei with the method used for Fig. 8 of Ref. [10]. 10^5 antinuclei are sufficient to probe the bin $\log_{10}(\mathcal{A}) \leq -2$. This figure confirms the effect of the turbulent Galactic magnetic field. As previously pointed out, the distributions tend to peak around the mean value $\mathcal{A} \sim 1$ and have lower variances for stronger and more extended turbulent components.

In addition, we can compute the maximum and minimum logarithmic amplifications $\log_{10}(\mathcal{A})$ on the whole sky. For the case without the turbulent field, we have $\log_{10}(\mathcal{A}) \approx 1.15$ for the maximum amplification. When including turbulent fields with the parameters ($B_0 = 1 \mu\text{G}$, $z_0 = 3$ kpc), ($B_0 = 4 \mu\text{G}$, $z_0 = 3$ kpc) and ($B_0 = 10 \mu\text{G}$, $z_0 = 10$ kpc), we respectively find that the maximum values for $\log_{10}(\mathcal{A})$ are ≈ 0.95 , ≈ 0.63 and ≈ 0.47 . For the case with $B_0 = 10 \mu\text{G}$ and $z_0 = 10$ kpc, the minimum value for $\log_{10}(\mathcal{A})$ is ~ -1.6 . For the other cases, the minimum amplifications are too low to be probed with only 10^5 backtraced antinuclei.

The larger the amplitude and extension of the turbulent GMF, the weaker the amplitude between the maximum magnification

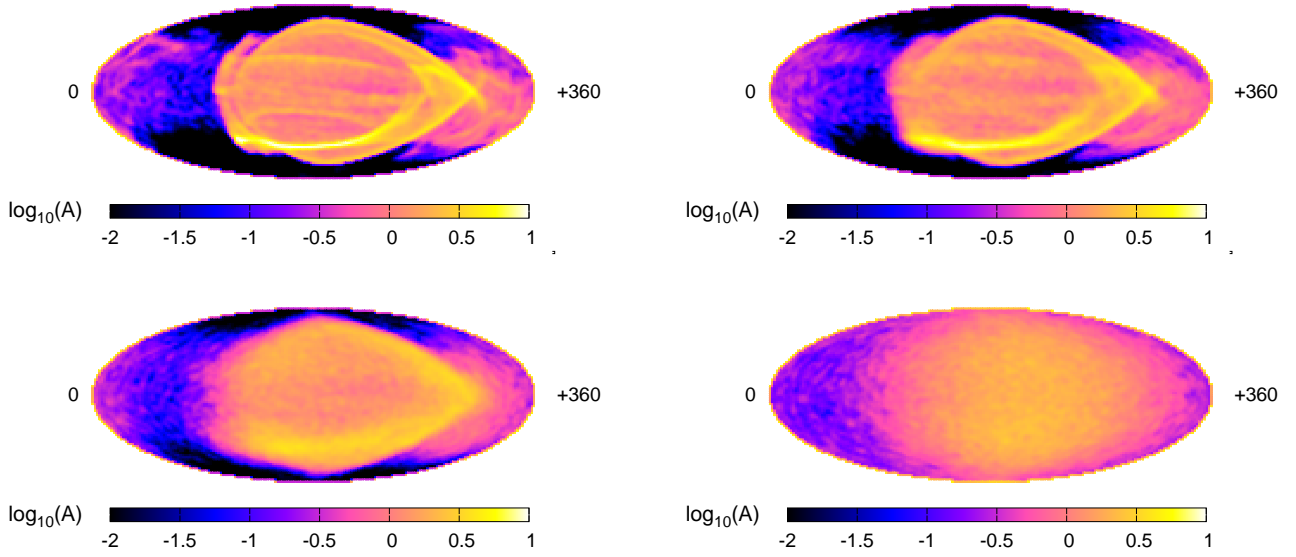


Figure 5: Logarithm of the amplification factor \mathcal{A} of the flux of extragalactic 60 EeV iron nuclei sources, depending on their position on the sky. Plots are in Galactic coordinates, with the Galactic anti-center in the center. We take the PS model for the regular component of the GMF. Regions with $\log_{10}(\mathcal{A}) \leq -2$ are in black. **Upper left panel:** No additional turbulent field component is added. The small fraction of the sky with $\log_{10}(\mathcal{A}) \geq 1$ is in white; **Upper right panel:** Additional turbulent field with $B_0 = 1 \mu\text{G}$, $L_c = 50 \text{ pc}$ and $z_0 = 3 \text{ kpc}$; **Lower left panel:** $B_0 = 4 \mu\text{G}$, $L_c = 50 \text{ pc}$ and $z_0 = 3 \text{ kpc}$; **Lower right panel:** $B_0 = 10 \mu\text{G}$, $L_c = 50 \text{ pc}$ and $z_0 = 10 \text{ kpc}$.

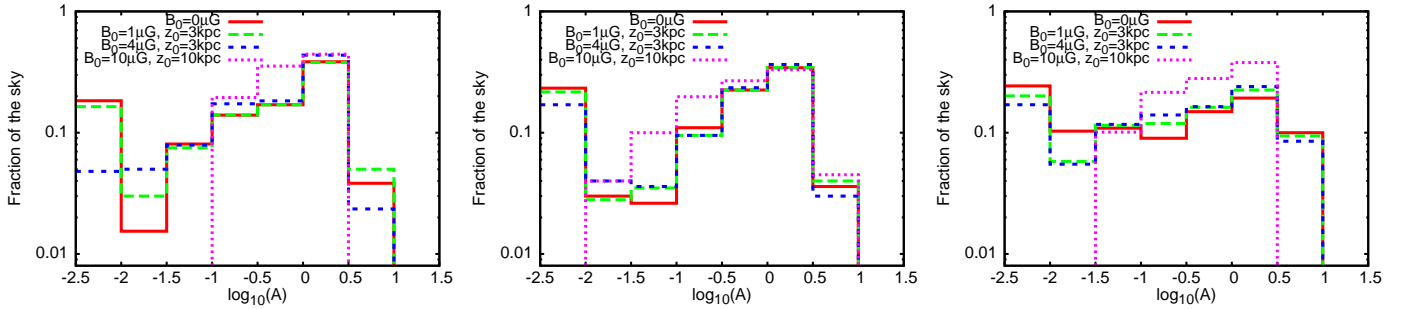


Figure 6: Histogram of fractions of the sky outside the Galaxy with amplifications \mathcal{A} within bins of width $\Delta \log_{10}(\mathcal{A}) = 0.5$. **Left panel:** For all four histograms, the GMF regular component is given by the PS model; **Middle panel:** Sun8 model –“ASS+RING” model of Ref. [27]; **Right panel:** Sun8-MH model, as defined in Ref. [10]. In each plot, solid red lines for no additional turbulent field component. Green, blue and magenta lines for the cases of a turbulent field with parameters respectively set to $(B_0 = 1 \mu\text{G}, z_0 = 3 \text{ kpc})$, $(B_0 = 4 \mu\text{G}, z_0 = 3 \text{ kpc})$ and $(B_0 = 10 \mu\text{G}, z_0 = 10 \text{ kpc})$. The correlation length L_c is 50 pc. The bin of amplifications \mathcal{A} below 10^{-2} corresponds to blind regions.

and demagnification. This result is in line with our previous findings.

The fraction of the sky covered by blind regions corresponds to the left-most bin of the diagram in Fig. 6 (left panel). Without taking into account the turbulent field, we find that blind regions encompass $\approx 18\%$ of the sky for the PS model. When including turbulent fields with the parameters $(B_0 = 1 \mu\text{G}, z_0 = 3 \text{ kpc})$, $(B_0 = 4 \mu\text{G}, z_0 = 3 \text{ kpc})$, $(B_0 = 10 \mu\text{G}, z_0 = 10 \text{ kpc})$, blind regions respectively represent $\approx 16\%$, $\approx 5\%$ and 0% of the sky. Therefore, if the turbulent component is strong and sufficiently extended in the z -direction, the fraction of blind regions on the sky can easily fall below 15%. However, this would not facilitate source searches due to the bigger spread and blurring of their images, cf. the previous section.

We test to which extent these results are generic. We show

in the two other panels of Fig. 6 the same diagrams for two other regular GMF models. In Fig. 6 (middle panel), we take the “ASS+RING” model of Reference [27], which we will call the “Sun8” model. In Fig. 6 (right panel), we use the modified version of the Sun8 model introduced in Ref. [10]. We call it the “Sun8-MH (Modified Halo)” model. The four diagrams correspond to the same turbulent field strengths and extensions in the halo, as in the left panel. One can see that the sizes of blind regions without turbulent field are very similar in the three models, though they decrease faster with increasing turbulent field contributions in the case of the PS model. The tendency is however generic: With increasing turbulent field strengths and extensions, the sizes of regions of extreme magnification and demagnification shrink and eventually disappear. The amplification distributions tend to peak more around the $\mathcal{A} \sim 1$ value.

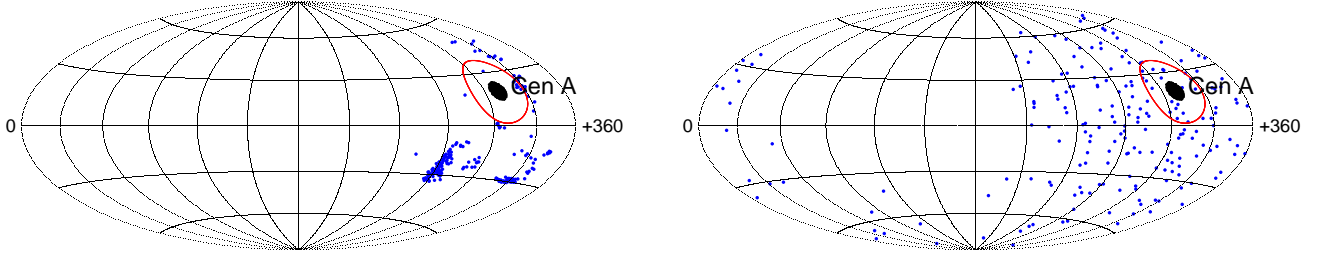


Figure 7: **Left panel:** Image of iron nuclei with $E \geq 55$ EeV emitted by Cen A, deflected in the PS regular GMF model only, and convolved with the Pierre Auger Observatory exposure; **Right panel:** Same as in the left panel, with an additional strong and extended turbulent Galactic magnetic field. The turbulent magnetic field has a Kolmogorov spectrum, with $L_c = 50$ pc, $B_0 = 10 \mu\text{G}$ and $z_0 = 10$ kpc. Sky maps in Galactic coordinates, with the anti-Galactic center in the center. Cosmic rays are in dark blue and the black disks denote the position of Cen A on the sky. The red circles surround the region within 18° from Cen A.

For all three regular GMF models, the green lines ($B_0 = 1 \mu\text{G}$, $z_0 = 3$ kpc) are still close to the red lines (no turbulent field), and the blue lines ($B_0 = 4 \mu\text{G}$, $z_0 = 3$ kpc) show a visible decrease of the sizes of the extreme (de-)magnification regions, as well as an increase of bins with more moderate \mathcal{A} . In all three panels, blind regions completely disappear for the largest turbulent field contribution ($B_0 = 10 \mu\text{G}$, $z_0 = 10$ kpc). All distributions are centered on moderate \mathcal{A} bins, but their widths depend on the regular GMF model. The width for the Sun08 model magenta distribution is larger than for those of the two other models. This is due to the large strength of this field in the halo - up to $10 \mu\text{G}$, which is comparable to that of the turbulent field. Regions with $-2 \leq \log_{10}(\mathcal{A}) \leq -1.5$ and with $0.5 \leq \log_{10}(\mathcal{A}) \leq 1$ indeed disappear when a more reasonable regular field strength in the halo is taken, such as for the Sun08-MH model.

5. Can all UHECR measured at Earth come from a sole nearby extragalactic source?

In this section we test the hypothesis that all UHECR detected at Earth may be due to one nearby source such as Cen A. Cen A has been suggested to be a source of UHECR since a long time [47, 48, 49].

Since we are sufficiently far from the most prominent objects of the nearby Large Scale Structure (LSS) and since Cen A is only 3.4 Mpc away and located within a relatively cold region of the local LSS, the extragalactic magnetic fields are unlikely to cause large deflections between Cen A and the Earth. We will neglect them in the following. Therefore, we only have to consider deflections in the GMF. We plot in Fig 7 (left panel) the image of Cen A emitting iron nuclei with $E \geq 55$ EeV, deflected in the PS regular GMF model only. The blue dots correspond to the arrival directions of such events, and the black disk denotes Cen A position on the sky. The image is convolved with the Pierre Auger Observatory exposure. We use the exposure formula of Ref. [50] with $\delta = -35.2^\circ$ for the Auger declination and $\theta_m = 60^\circ$ for its maximum zenith angle. We backtrace antinuclei from the Earth to outside the Galaxy, with initial directions following the exposure. The antinuclei energies follow the energies of the 69 events published by the Pierre Auger Collaboration [5]. Once the antinuclei leave the Galaxy, we save those with escape directions on the sky within 5 degrees from

the center of Cen A. This corresponds to assuming that Cen A is a $\sim 5^\circ$ extended source. We could have used more realistic geometries than a disk, but this would not significantly change our conclusions.

Reference [5] discussed the $\approx 18^\circ$ radius overdensity of events with $E \geq 55$ EeV around Cen A, and Ref. [51] found that when removing this overdense region, the rest of the sky above 55 EeV is still compatible with isotropy. This region is surrounded with red circles in Fig 7. Refs. [52, 53] suggested that the overdensity may be the heavy nuclei image of Cen A. Fig 7 (left panel) shows that in the PS regular GMF model, the images of Cen A are deflected beyond the $\approx 18^\circ$ radius region around Cen A. In all other tested models, heavy nuclei are also shifted by at least a few tens of degrees from Cen A. However, this result is model-dependent and one cannot rule out the hypothesis of Refs. [52, 53] yet. Reference [54] suggested that the overdensity around Cen A may be explained by light nuclei emitted by Cen A. The distance to Cen A is small enough to avoid problems with photo-disintegration. References [51, 55] proposed that this overdensity may be the image of Virgo emitting heavy nuclei, shifted by the regular GMF.

Fig. 7 (left panel) shows that iron nuclei emitted by Cen A cannot be sufficiently spread over the whole sky in regular GMF models to explain *all* Auger data above 55 EeV. Moreover, we have seen in Section 3 that for the ranges of turbulent component parameters used there, ~ 60 EeV iron nuclei would not be spread over the whole celestial sphere. Therefore, the only potential way for the one source hypothesis to be true is that the turbulent GMF is very strong and extended. We choose as an extreme case $B_0 = 10 \mu\text{G}$ and $z_0 = 10$ kpc. We assume the turbulent field has a Kolmogorov spectrum with $L_c = 50$ pc. These values for the strength and the extension of this field are deliberately larger than the maximum values one can find in the literature. For example, one of the largest values proposed for z_0 is $z_0 \sim 7$ kpc [56].

Blue dots in Fig. 7 (right panel) show the arrival directions of iron nuclei with $E \geq 55$ EeV emitted by Cen A, when this extreme turbulent component is added to the PS model. The Cen A image is convolved with the Pierre Auger exposure. Since deflections are dominated by the turbulent GMF in this case, using another reasonable model for the regular GMF would not noticeably affect the results presented below. Due to

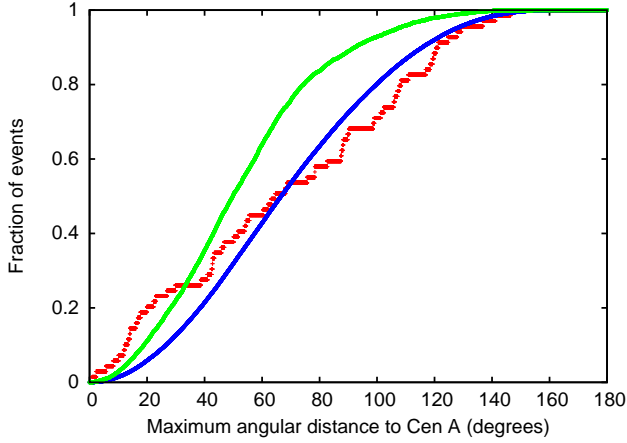


Figure 8: Fractions of cosmic rays within a given angular distance (in degrees) to Cen A. Blue distribution for isotropic arrival directions, red one for the 69 Auger events published in Ref [5], and green one for iron nuclei with $E \geq 55$ EeV emitted by Cen A and deflected in the Galactic magnetic field model considered for Fig. 7 (right panel). Both blue and green distributions take into account the exposure of the Pierre Auger experiment.

computing time reasons, we used in this section a turbulent field generated via the FFT method, see Section 2 for more details. In order to have sufficient statistics for the following study, we backtraced 3.6×10^6 particles from the Earth.

The turbulent field starts to be sufficiently strong to spread the arrival directions of Cen A nuclei over the whole celestial sphere. However, even with such a field, the arrival directions of cosmic rays still display a non-negligible dipolar pattern on the sky. The density of cosmic ray arrival directions is larger in the half-sky centered on Cen A than in the opposite half-sky. This tends to be in conflict with the angular distribution found from the observational data.

In Fig. 8 we draw the distributions of the fractions of cosmic rays within given angular distances from Cen A, both for the published Pierre Auger data with $E \geq 55$ EeV [5] ($N_1 = 69$ events) and for $N_2 \simeq 6300$ cosmic rays emitted by Cen A and deflected in our extreme GMF model. These two distributions are respectively represented by the red and green curves in Figure 8. The blue curve on the same panel corresponds to the case of isotropic arrival directions of cosmic rays (computed with $N_2 = 10^5$ events). Both blue and green lines take into account the exposure of the Pierre Auger experiment. The green line is always above the blue one. This confirms the presence of a non-zero dipolar pattern in the arrival directions of the cosmic rays emitted by Cen A.

We verify with a Kolmogorov-Smirnov test [35] that the hypothesis that all cosmic rays are emitted by Cen A (green distribution) is not compatible with the Pierre Auger data [5] (red distribution). This test consists in measuring the maximum distance d_{\max} between the two distributions. The significance level of the observed value d_{\max} , $P(d_{\max} > \text{observed})$, is directly inferred from d_{\max} , N_1 and N_2 [35]. The maximum distance between the red and green curves is $d_{\max} \simeq 0.28$, at an angular distance to Cen A $d_{\text{CenA}} \simeq 87^\circ$. It corresponds to a probability $P(d_{\max} > \text{observed}) \sim (2 - 4) \times 10^{-5}$.

For a weaker or less extended turbulent GMF than the extreme case considered here, events would be less spread on the sky, and the probability $P(d_{\max} > \text{observed})$ would be even lower. Therefore, the hypothesis that Cen A is the sole UHECR accelerator seen at Earth at the highest energies is strongly disfavoured by the Pierre Auger data, even if we consider the most favourable case of a heavy composition and a very strong turbulent GMF component.

6. Conclusions and perspectives

In the present paper, we have investigated the consequences of a turbulent GMF component on the propagation of UHECRs for the case of a heavy composition at the highest energies. We have backtraced 60 EeV iron antinuclei in GMF models including both a regular and a turbulent component. For the regular component we have mostly used the Prouza and Smida (PS) model as a generic example representative for regular GMF models. We have tested the model-dependence of our results by also considering the Sun08 and Sun08-MH models, as in Ref. [10]. We have varied the parameters describing the turbulent field, accounting thereby for the poor knowledge of its properties.

In Section 3, we have computed the 60 EeV iron images of the Fornax galaxy cluster and of the supergalactic plane. We have shown qualitatively to which extent the turbulent component may spread these images. We have also discussed the dependence of such a spread on the turbulent GMF parameters.

In Section 4, we have shown that the presence of a turbulent field tends to reduce the extreme (de-) magnification of individual source fluxes. We have called “blind regions” those parts of the sky in which the flux of UHECR sources is demagnified by more than a factor 100. Current and next generation experiments will not be able to detect sources located in such regions. The size of these regions shrinks when including the effect of a turbulent GMF: At 60 EeV, for sufficiently strong turbulent field strengths of $\simeq 4 \mu\text{G}$ at Earth and large extensions $\gtrsim 3$ kpc into the halo, the fraction of blind regions was reduced by more than a factor 3 in the case of the PS regular GMF model.

In the last section, we tested the hypothesis that all UHECR detected at Earth above $\simeq 55$ EeV could be due to a sole nearby source, such as Cen A. We found that, even in the most favourable case of iron nuclei deflected in a strong and extended GMF turbulent component, this scenario is not compatible with the present data of the Pierre Auger experiment.

Finally we note that future radio experiments, such as LOFAR and SKA, will improve our knowledge of the properties of the GMF turbulent component, such as its strength and its extension in the Galactic halo [57, 58].

Acknowledgments

This work was supported by the Deutsche Forschungsgemeinschaft through the collaborative research centre SFB 676. GS and GG acknowledge support from the State of Hamburg,

through the Collaborative Research program “Connecting Particles with the Cosmos” within the framework of the LandesExzellenzInitiative (LEXI).

References

- [1] R. U. Abbasi *et al.* [HiRes Collaboration], Phys. Rev. Lett. **100**, 101101 (2008) [arXiv:astro-ph/0703099]; R. U. Abbasi *et al.*, Astropart. Phys. **32**, 53 (2009) [arXiv:0904.4500 [astro-ph.HE]].
- [2] J. Abraham *et al.* [Pierre Auger Collaboration], Phys. Rev. Lett. **101**, 061101 (2008) [arXiv:0806.4302 [astro-ph]].
- [3] J. Abraham *et al.* [The Pierre Auger Collaboration], Phys. Lett. B **685**, 239 (2010) [arXiv:1002.1975 [astro-ph.HE]].
- [4] J. Abraham *et al.* [Pierre Auger Collaboration], Science **318**, 938 (2007) [arXiv:0711.2256 [astro-ph]]; J. Abraham *et al.* [Pierre Auger Collaboration], Astropart. Phys. **29**, 188 (2008) [Erratum-ibid. **30**, 45 (2008)] [arXiv:0712.2843 [astro-ph]].
- [5] P. Abreu *et al.* [Pierre Auger Observatory Collaboration], Astropart. Phys. **34**, 314-326 (2010). [arXiv:1009.1855 [astro-ph.HE]].
- [6] J. Abraham *et al.* [Pierre Auger Observatory Collaboration], Phys. Rev. Lett. **104**, 091101 (2010). [arXiv:1002.0699 [astro-ph.HE]].
- [7] A. V. Glushkov, I. T. Makarov, M. I. Pravdin, I. E. Slepsov, D. S. Gorbunov, G. I. Rubtsov and S. V. Troitsky, JETP Lett. **87**, 190 (2008) [arXiv:0710.5508 [astro-ph]].
- [8] J. Belz *et al.*, for the HiRes Collaboration, “Composition Studies using Depth of Shower Maximum with the High-Resolution Fly’s Eye (HiRes),” in *Proc. “31st International Cosmic Ray Conference”, Łódź, Poland, 2009*.
- [9] Y. Tameda *et al.* [Telescope Array Collaboration], “Preliminary results of Telescope Array”, talk at the Japanese Physical Society meeting, March 26, 2010.
- [10] G. Giacinti, M. Kachelrieß, D. V. Semikoz and G. Sigl, JCAP **1008**, 036 (2010) [arXiv:1006.5416 [astro-ph.HE]].
- [11] T. Stanev, Astrophys. J. **479**, 290 (1997) [arXiv:astro-ph/9607086].
- [12] D. Harari, S. Mollerach and E. Roulet, JHEP **9908**, 022 (1999) [arXiv:astro-ph/9906309].
- [13] P. G. Tinyakov and I. I. Tkachev, Astropart. Phys. **18**, 165 (2002) [arXiv:astro-ph/0111305].
- [14] J. P. Vallee, Astrophys. J. **681**, 303 (2008).
- [15] L. Page *et al.* [WMAP Collaboration], Astrophys. J. Suppl. **170**, 335 (2007) [arXiv:astro-ph/0603450].
- [16] J. C. Brown *et al.*, Astrophys. J. **663**, 258 (2007) [arXiv:0704.0458 [astro-ph]].
- [17] Y. Y. Jiang, L. G. Hou, J. L. Han, X. H. Sun and W. Wang, Astrophys. J. **719**, 459 (2010) [arXiv:1004.1877 [astro-ph.HE]].
- [18] L. G. Hou, J. L. Han and W. B. Shi, “The spiral structure of our Milky Way Galaxy,” arXiv:0903.0721 [astro-ph.GA].
- [19] J. L. Han, R. N. Manchester, A. G. Lyne, G. J. Qiao and W. van Straten, Astrophys. J. **642**, 868 (2006) [arXiv:astro-ph/0601357].
- [20] J. L. Han, Nucl. Phys. Proc. Suppl. **175**, 62 (2008) [arXiv:0901.0040 [astro-ph.GA]].
- [21] J. L. Han, “Magnetic structure of our Galaxy: A review of observations,” arXiv:0901.1165 [astro-ph].
- [22] K. Rae and J. A. Brown, “Constraints on the Galactic Magnetic Field from the Canadian Galactic Plane Survey,” arXiv:1012.2934 [astro-ph.GA].
- [23] C. Van Eck and J. A. Brown, “Modeling the Galactic Magnetic Field using Rotation Measure Observations in the Galactic Disk from the CGPS, SGPS, and the VLA,” arXiv:1012.2936 [astro-ph.GA].
- [24] C. Van Eck *et al.*, Astrophys. J. **728**, 97 (2011) [arXiv:1012.2938 [astro-ph.GA]].
- [25] M. Prouza and R. Smida, Astron. Astrophys. **410** (2003) 1 [arXiv:astro-ph/0307165].
- [26] M. Kachelrieß, P. D. Serpico and M. Teshima, Astropart. Phys. **26**, 378 (2006) [arXiv:astro-ph/0510444].
- [27] X. H. Sun, W. Reich, A. Waelkens and T. Enßlin, Astron. Astrophys. **477**, 573 (2008) [arXiv:0711.1572 [astro-ph]].
- [28] X. Sun and W. Reich, Res. Astron. Astrophys. **10**, 1287 (2010) [arXiv:1010.4394 [astro-ph.GA]].
- [29] M. S. Pshirkov, P. G. Tinyakov, P. P. Kronberg and K. J. Newton-McGee, Astrophys. J. **738**, 192 (2011) [arXiv:1103.0814 [astro-ph.GA]].
- [30] R. Jansson, G. R. Farrar, A. H. Waelkens and T. A. Enßlin, JCAP **0907**, 021 (2009) [arXiv:0905.2228 [astro-ph.GA]].
- [31] A. Waelkens, T. Jaffe, M. Reinecke, F. S. Kitaura and T. A. Enßlin, Astron. Astrophys. **495**, 697 (2009) [arXiv:0807.2262 [astro-ph]].
- [32] D. Harari, S. Mollerach, E. Roulet and F. Sanchez, JHEP **0203**, 045 (2002) [arXiv:astro-ph/0202362].
- [33] P. G. Tinyakov and I. I. Tkachev, Astropart. Phys. **24**, 32 (2005) [arXiv:astro-ph/0411669].
- [34] J. Giacalone and J. R. Jokipii, Astrophys. J. **520**, 204 (1999).
- [35] W. H. Press, S. A. Teukolsky, W. T. Vetterling, B. P. Flannery, *Numerical Recipes in C: The Art of Scientific Computing, Second Edition*, Cambridge University Press (1992).
- [36] G. Giacinti, X. Derkx and D. V. Semikoz, JCAP **1003**, 022 (2010) [arXiv:0907.1035 [astro-ph.HE]].
- [37] G. Golup, D. Harari, S. Mollerach and E. Roulet, Astropart. Phys. **32**, 269 (2009) [arXiv:0902.1742 [astro-ph.HE]].
- [38] D. Harari, S. Mollerach and E. Roulet, JHEP **0002**, 035 (2000) [arXiv:astro-ph/0001084].
- [39] D. Harari, S. Mollerach and E. Roulet, JHEP **0010**, 047 (2000) [arXiv:astro-ph/0005483].
- [40] K. Dolag, D. Grasso, V. Springel and I. Tkachev, JETP Lett. **79**, 583 (2004) [Pisma Zh. Eksp. Teor. Fiz. **79**, 719 (2004)] [arXiv:astro-ph/0310902].
- [41] K. Dolag, D. Grasso, V. Springel and I. Tkachev, JCAP **0501**, 009 (2005) [arXiv:astro-ph/0410419].
- [42] G. Sigl, F. Miniati and T. A. Ensslin, Phys. Rev. D **70**, 043007 (2004) [arXiv:astro-ph/0401084].
- [43] S. Das, H. Kang, D. Ryu and J. Cho, “Propagation of UHE Protons through Magnetized Cosmic Web,” arXiv:0801.0371 [astro-ph].
- [44] D. Ryu, S. Das and H. Kang, Astrophys. J. **710**, 1422 (2010) [arXiv:0910.3361 [astro-ph.HE]].
- [45] G. Sigl, F. Miniati and T. Ensslin, Nucl. Phys. Proc. Suppl. **136**, 224 (2004) [arXiv:astro-ph/0409098].
- [46] K. Dolag, M. Kachelrieß and D. V. Semikoz, JCAP **0901**, 033 (2009) [arXiv:0809.5055 [astro-ph]].
- [47] G. Cavallo, Astron. Astrophys. **65** 415 (1978).
- [48] G. E. Romero, J. A. Combi, L. A. Anchordoqui and S. E. Perez Bergliaffa, Astropart. Phys. **5**, 279 (1996) [arXiv:gr-qc/9511031].
- [49] L. A. Anchordoqui, H. Goldberg and T. J. Weiler, Phys. Rev. Lett. **87**, 081101 (2001) [arXiv:astro-ph/0103043].
- [50] P. Sommers, Astropart. Phys. **14**, 271 (2001) [arXiv:astro-ph/0004016].
- [51] D. V. Semikoz, “Ultrahigh energy nuclei source in the direction to Virgo cluster,” arXiv:1009.3879 [astro-ph.HE].
- [52] D. Gorbunov, P. Tinyakov, I. Tkachev and S. V. Troitsky, JETP Lett. **87**, 461 (2008) [arXiv:0711.4060 [astro-ph]].
- [53] D. S. Gorbunov, P. G. Tinyakov, I. I. Tkachev and S. V. Troitsky, “On the interpretation of the cosmic-ray anisotropy at ultrahigh energies,” arXiv:0804.1088 [astro-ph].
- [54] D. Fargion, Phys. Scripta **78**, 045901 (2008) [arXiv:0801.0227 [astro-ph]].
- [55] G. Giacinti and D. V. Semikoz, Phys. Rev. D **83**, 083002 (2011) [arXiv:1011.6333 [astro-ph.HE]].
- [56] R. Beck, AIP Conf. Proc. **1085**, 83 (2009) [arXiv:0810.2923 [astro-ph]].
- [57] B. M. Gaensler, R. Beck and L. Feretti, New Astron. Rev. **48**, 1003 (2004) [arXiv:astro-ph/0409100].
- [58] R. Beck and B. M. Gaensler, New Astron. Rev. **48**, 1289 (2004) [arXiv:astro-ph/0409368].